Ann. Geophys., 34, 1165–1173, 2016
www.ann-geophys.net/34/1165/2016/
doi:10.5194/angeo-34-1165-2016

Annales Geophysicae Open Access EGU

Euler potentials for two layers with non-constant current densities in the ambient magnetic field aligned to the layers

Marek Vandas[1] **and Eugene P. Romashets**[2]

[1]Astronomical Institute of the Czech Academy of Sciences, Boční 1401, 14100 Prague 4, Czech Republic
[2]University Park, LSC, Houston, TX 77095, USA

Correspondence to: Marek Vandas (vandas@asu.cas.cz)

Received: 4 May 2016 – Revised: 2 November 2016 – Accepted: 15 November 2016 – Published: 13 December 2016

Abstract. The Euler potentials for two current layers aligned to an ambient homogeneous magnetic field are found. Previous treatment of such a system assumed constant current density in the layers. However, the magnetic field becomes infinite at the edges. The new approach eliminates this inconsistency by introducing an inhomogeneous current density. Euler potentials are constructed semi-analytically for such a system. Charged-particle motion and trapping in it are examined by this representation. Using Euler potentials, the influence of current sheets of zero and non-zero thicknesses on energetic-particle fluxes is investigated, and characteristic flux variations near the sheets are presented. The results can be applied to Birkeland currents.

Keywords. Magnetospheric physics (current systems)

1 Introduction

Euler potentials represent an alternative way of describing a magnetic field. They are two scalar functions, usually denoted as α and β, related to the magnetic field vector by

$$\boldsymbol{B} = \operatorname{grad}\alpha \times \operatorname{grad}\beta. \quad (1)$$

Such a relationship relies on the fact that magnetic fields are always solenoidal; that is, they fulfill the condition $\operatorname{div}\boldsymbol{B} = 0$. The potentials bear their name of Leonhard Euler (Euler, 1769), who introduced them for investigation of incompressible flows where it holds that $\operatorname{div}\boldsymbol{V} = 0$. Replacing the bulk velocity $\boldsymbol{V}$ by $\boldsymbol{B}$, Sweet (1950) applied the theory of Euler potentials to magnetic field systems. Euler potentials are explicitly known mainly for simple magnetic field systems, e.g., a dipole field (Stern, 1966; Webb et al., 2010). From the definition (Eq. 1) it is clear that Euler potentials are not unique, but they are constant along magnetic field lines. This property makes them a convenient tool for studies of charged-particle motions in related magnetic fields (Gardner, 1959; Northrop and Teller, 1960; Ray, 1963). In recent years they are applied to a description of magnetic fields and charged-particle dynamics in Earth's magnetosphere–ionosphere (Schulz and Chen, 2008; Zaharia, 2008; Gkioulidou et al., 2012; Wang et al., 2014).

Romashets and Vandas (2012) have analytically obtained Euler potentials for a system where electric currents in two sheets flow along background magnetic field lines, that is, for situations relevant to Birkeland currents in the auroral magnetosphere–ionosphere. Birkeland currents are currents flowing along magnetic field lines in two sheets (Schield et al., 1969; Vasyliunas, 1970; Russell and Fleishman, 2002). Originally deduced from ground-based magnetic field variation measurements during auroral phenomena, they were confirmed by in situ measurements in the 1970s (Zmuda and Armstrong, 1974; Iijima and Potemra, 1976a, b). Current observations enable the construction of maps of Birkeland currents in detail (e.g., Friis-Christensen and Lassen, 1991; Russell et al., 1997; Waters et al., 2001; Korth et al., 2010; Anderson et al., 2014). The model by Romashets and Vandas (2012) was simple: current sheets had zero thickness and uniform current distribution inside them. This system has a feature which is unnatural; that is, the magnetic field diverges (becomes infinite) at the sheet edges. In order to fix this unwanted property, Vandas and Romashets (2014) introduced a non-zero thickness of the sheets. However, for small thicknesses of the sheets (which are relevant to Birkeland currents) the magnetic field at the edges becomes too high because this system resembles a zero-thickness sheet configu-

ration. In this paper we propose an alternative way of fixing the field divergence: the sheets will retain their zero thickness, but the distribution of the current inside them will not be uniform. Section 2 describes derivation of Euler potentials for two current sheets aligned with a uniform ambient magnetic field. In Sect. 3 new results are compared to the case of sheets with uniform currents and similarities/differences are outlined. Section 4 uses derived Euler potentials to investigate the influence of current sheets on energetic-particle fluxes.

2 Euler potentials

Figure 1a shows the considered current system. Two sheets with varying surface current density are situated parallel to the z axis, they are boundless along it, they are separated by $2x_0$ in the x direction, and extend by $2y_0$ in the y direction. The currents in the sheets can be parallel or anti-parallel to each other: denoting the surface current density at the right sheet by $\boldsymbol{j}$, the left sheet will have $\pm\boldsymbol{j}$ for the same y (the "±" nomenclature will be used throughout this section and means parallel, "+", or anti-parallel, "−", cases). The surface current density in the right sheet is constant and equal to $j_0 > 0$ within $|y| < y_1$ ($0 < y_1 < y_0$) and then linearly decreases to zero towards the edges ($y = y_0$ or $y = -y_0$), so its profile is trapezoidal (see Fig. 2).

First we consider one sheet only and centered at the origin. The magnetic field is determined from the Biot–Savart law:

$$\boldsymbol{B}(\boldsymbol{r}) = \frac{\mu_0}{4\pi} \int \frac{\boldsymbol{j}(\boldsymbol{r}') \times (\boldsymbol{r} - \boldsymbol{r}')}{|\boldsymbol{r} - \boldsymbol{r}'|^3} \, \mathrm{d}S. \tag{2}$$

In our case we have $\boldsymbol{j} = j(y)\boldsymbol{e}_z$, where $\boldsymbol{e}_z$ is the unit vector in the direction of the z axis, so

$$\boldsymbol{B}^{(1)}(x, y, z) = \frac{\mu_0}{2\pi} \int_{-y_0}^{y_0} \frac{[(y' - y)j(y'), xj(y'), 0]}{x^2 + (y' - y)^2} \, \mathrm{d}y', \tag{3}$$

where the integration over z' has already been performed. Assuming the trapezoidal surface current profile (Fig. 2), the resulting field becomes

$$\begin{aligned} B_x^{(1)} = B_i \frac{x_0}{y_0 + y_1} \Bigg[& \frac{x}{y_0 - y_1} \left(\arctan \frac{y + y_1}{x} + \arctan \frac{y - y_1}{x} \right. \\ & \left. - \arctan \frac{y + y_0}{x} - \arctan \frac{y - y_0}{x} \right) \\ & + \frac{1}{2} \ln \frac{x^2 + (y - y_1)^2}{x^2 + (y + y_1)^2} - \frac{y + y_0}{2(y_0 - y_1)} \\ & \times \ln \frac{x^2 + (y + y_0)^2}{x^2 + (y + y_1)^2} - \frac{y - y_0}{2(y_0 - y_1)} \ln \frac{x^2 + (y - y_0)^2}{x^2 + (y - y_1)^2} \Bigg], \end{aligned} \tag{4}$$

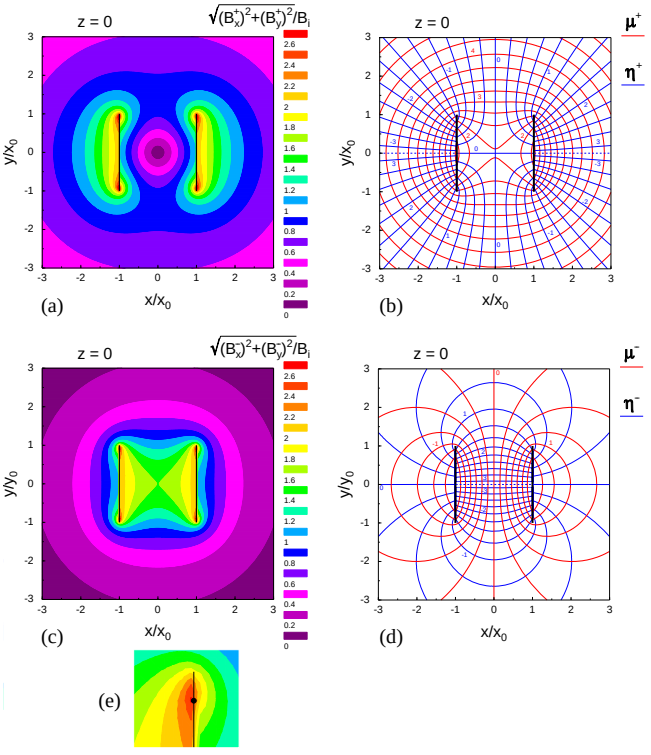

Figure 1. Upper panels: **(a)** magnetic field magnitude distribution without the ambient field B_0 and **(b)** the orthogonal coordinates in the $z = 0$ plane for the parallel case when $y_0 = x_0$ and $y_1 = 0.9y_0$. Middle panels: the same **(c)** magnetic field magnitude and **(d)** coordinates, for the anti-parallel case. The coordinates $\mu^{\pm}$ are plotted by thick red lines and the coordinates $\eta^{\pm}$ by thin blue lines. The two thick vertical black lines in each panel, stretching from −1 to 1, are current sheets. Panel **(e)** is a magnified part of panel **(c)** around the right top sheet edge, and it is discussed in Sect. 3.

$$\begin{aligned} B_y^{(1)} = B_i \frac{x_0}{y_0 + y_1} \Bigg\{ & \arctan \frac{y + y_1}{x} - \arctan \frac{y - y_1}{x} \\ & + \frac{y + y_0}{y_0 - y_1} \left(\arctan \frac{y + y_0}{x} - \arctan \frac{y + y_1}{x} \right) \\ & + \frac{y - y_0}{y_0 - y_1} \left(\arctan \frac{y - y_0}{x} - \arctan \frac{y - y_1}{x} \right) \\ & - \frac{x}{2(y_0 - y_1)} \ln \frac{[x^2 + (y + y_0)^2][x^2 + (y - y_0)^2]}{[x^2 + (y + y_1)^2][x^2 + (y - y_1)^2]} \Bigg\}, \end{aligned} \tag{5}$$

$$B_z^{(1)} = 0, \tag{6}$$

where B_i is introduced via the total current I_0 of the sheet, $B_i = \mu_0 I_0/(2\pi x_0)$ and $I_0 = j_0(y_0 + y_1)$ (μ_0 is the magnetic vacuum permeability).

One can verify that the boundary conditions for the magnetic field at the current sheet are satisfied. They generally read $\boldsymbol{n} \cdot (\boldsymbol{B}_2 - \boldsymbol{B}_1) = 0$ and $\boldsymbol{n} \times (\boldsymbol{B}_2 - \boldsymbol{B}_1) = \mu_0 \boldsymbol{j}$, where $\boldsymbol{n}$ is a unit normal vector to the boundary pointing from region 1

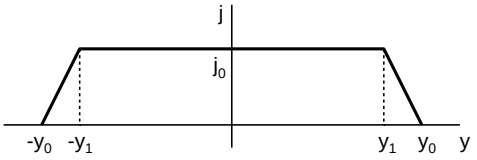

Figure 2. Profile of the surface current density j along a sheet.

to region 2, and $\boldsymbol{j}$ is the surface current flowing on the boundary. In our case if region 1 has $x < 0$ and $|y| < y_0$, we have $\boldsymbol{n} = (1, 0, 0)$, $\boldsymbol{B}_1 = \lim_{x\to 0-} \boldsymbol{B}^{(1)}$, and $\boldsymbol{B}_2 = \lim_{x\to 0+} \boldsymbol{B}^{(1)}$. Direct calculations using Eqs. (4)–(6) prove that the boundary conditions are met.

Magnetic field at the edge is

$$\begin{aligned}\boldsymbol{B}^{(1)}_{\text{edge}} &= \lim_{y\to y_0+}\lim_{x\to 0} \boldsymbol{B}^{(1)}(x, y, z)\\ &= B_i \frac{x_0}{y_0 + y_1}\left\{\ln\left(\frac{2y_0}{y_0 + y_1} - 1\right)\right.\\ &\left. -\frac{2y_0}{y_0 - y_1}\ln\frac{2y_0}{y_0 + y_1}, 0, 0\right\}. \end{aligned} \tag{7}$$

It is limited but for case of the uniform current density

$$\boldsymbol{B}^{(1u)}_{\text{edge}} = \lim_{y_1\to y_0} \boldsymbol{B}^{(1)}_{\text{edge}} = (-\infty, 0, 0). \tag{8}$$

Magnetic field of our system is given by

$$\boldsymbol{B}^{\pm}(x, y, z) = \boldsymbol{B}^{(1)}(x+x_0, y, z) \pm \boldsymbol{B}^{(1)}(x-x_0, y, z) + \boldsymbol{B}_0 \tag{9}$$

with the ambient homogeneous field $\boldsymbol{B}_0 = (0, 0, B_0)$. It follows from the fact that the Biot–Savart law is linear in currents, so the field from more currents is simply a superposition of the fields generated by the particular currents. We have two currents in the system, and the integral (Eq. 2) splits into two integrals, the first one for the left sheet with $x' = -x_0$ and the second one for the right sheet with $x' = x_0$. The boundary conditions at the sheets are met. Let us consider the right sheet. The magnetic field generated by the current here fulfills the boundary conditions as it has been already shown. The field from the left sheet and the homogeneous field $\boldsymbol{B}_0$ are continuous here, so they give no contributions to jumps.

When $y_1 \to y_0$, the field (Eq. 9) tends to the uniform current case (Romashets and Vandas, 2012). When $y_1 \to 0$, the current has a triangular profile. Figure 1a and c show magnetic field magnitude distribution without the ambient field B_0 when $y_0 = x_0$ and $y_1 = 0.9y_0$ for the parallel and antiparallel cases, respectively. The thick vertical lines depict two current sheets stretching from $y = -y_0$ to y_0 at $x = -x_0$ and $x = x_0$, respectively. The magnetic field magnitude remains limited at the edges of the sheets ($y = y_0$ or $y = -y_0$).

First we search Euler potentials $\alpha^{(1)}$ and $\beta^{(1)}$ for one current sheet centered at the origin and without the external field ($B_0 = 0$), that is, for the field given by Eqs. (4)–(6). We set

$$\alpha^{(1)} = B_i x_0 z \tag{10}$$

and from the definition of Euler potentials we have

$$\begin{aligned}\boldsymbol{B}^{(1)} &= \operatorname{grad}\alpha^{(1)} \times \operatorname{grad}\beta^{(1)}\\ &= B_i x_0\left(-\frac{\partial\beta^{(1)}}{\partial y}, \frac{\partial\beta^{(1)}}{\partial x}, 0\right),\end{aligned} \tag{11}$$

so we can calculate

$$\begin{aligned}\beta^{(1)} &= -\frac{1}{B_i x_0}\int B^{(1)}_x \,\mathrm{d}y\\ &= \frac{1}{4(y_0^2 - y_1^2)}\left\{4x\left[(y + y_0)\arctan\frac{y + y_0}{x}\right.\right.\\ &+ (y - y_0)\arctan\frac{y - y_0}{x} - (y + y_1)\arctan\frac{y + y_1}{x}\\ &\left. -(y - y_1)\arctan\frac{y - y_1}{x}\right]\\ &+ (x^2 - y^2)\ln\frac{[x^2 + (y + y_1)^2][x^2 + (y - y_1)^2]}{[x^2 + (y + y_0)^2][x^2 + (y - y_0)^2]}\\ &+ 2y\left[y_0\ln\frac{x^2 + (y + y_0)^2}{x^2 + (y - y_0)^2} - y_1\ln\frac{x^2 + (y + y_1)^2}{x^2 + (y - y_1)^2}\right]\\ &+ y_0^2\ln\frac{[x^2 + (y + y_0)^2][x^2 + (y - y_0)^2]}{x_0^4}\\ &\left. - y_1^2\ln\frac{[x^2 + (y + y_1)^2][x^2 + (y - y_1)^2]}{x_0^4}\right\} - \frac{1}{2}.\end{aligned} \tag{12}$$

The x_0 in denominators here has only the function to keep arguments dimensionless and to ensure that, in the limit $y_1 \to y_0$, the potential $\beta^{(1)}$ tends to that in Romashets and Vandas (2012).

We construct a set of curvilinear orthogonal coordinates $\mu^{(1)}$ and $\eta^{(1)}$. It is supposed that

$$\frac{\partial\mu^{(1)}}{\partial x} = -\frac{\partial\eta^{(1)}}{\partial y}, \quad \frac{\partial\mu^{(1)}}{\partial y} = \frac{\partial\eta^{(1)}}{\partial x} \tag{13}$$

and set $\mu^{(1)} = \beta^{(1)}$. The coordinates will be orthogonal because it is a vacuum field (cf. Vandas and Romashets, 2014, Appendix A). We have from Eqs. (13) and (11)

$$\begin{aligned}\eta^{(1)} &= \int\frac{\partial\mu^{(1)}}{\partial y}\,\mathrm{d}x = \int\frac{\partial\beta^{(1)}}{\partial y}\,\mathrm{d}x = -\frac{1}{B_i x_0}\int B^{(1)}_x\,\mathrm{d}x\\ &= \frac{1}{2(y_0^2 - y_1^2)}\left\{[x^2 - (y + y_0)^2]\arctan\frac{y + y_0}{x}\right.\\ &+[x^2 - (y - y_0)^2]\arctan\frac{y - y_0}{x} - [x^2 - (y + y_1)^2]\arctan\frac{y + y_1}{x}\\ &-[x^2 - (y - y_1)^2]\arctan\frac{y - y_1}{x} + x\left[(y + y_0)\ln\frac{x^2 + (y + y_0)^2}{x^2 + (y + y_1)^2}\right.\\ &+(y - y_0)\ln\frac{x^2 + (y - y_0)^2}{x^2 + (y - y_1)^2}\\ &\left.\left.+(y_0 - y_1)\ln\frac{x^2 + (y + y_1)^2}{x^2 + (y - y_1)^2}\right]\right\}.\end{aligned} \tag{14}$$

The curvilinear coordinates of the system of two current sheets (plus $\boldsymbol{B}_0$) are

$$\mu^{\pm}(x, y) = \mu^{(1)}(x + x_0, y) \pm \mu^{(1)}(x - x_0, y) \tag{15}$$

$$\eta^{\pm}(x,y) = \eta^{(1)}(x+x_0,y) \pm \eta^{(1)}(x-x_0,y) + k^{\pm}\pi, \quad (16)$$

$$\begin{aligned} k^+ &= 0 && |x| < x_0, \\ &= \text{sign } xy && |x| > x_0, \\ k^- &= \text{sign } y && |x| < x_0, \\ &= 0 && |x| > x_0, \end{aligned}$$

where sign is the signum function. In the limit $y_1 \to y_0$ (uniform current case) the coordinates $\mu^{\pm}$ and $\eta^{\pm}$ transform into the coordinates by the same symbols in Romashets and Vandas (2012). It holds that

$$\mu^+(-x,y) = \mu^+(x,y),\ \mu^-(-x,y) = -\mu^-(x,y),$$
$$\mu^{\pm}(x,-y) = \mu^{\pm}(x,y),$$
$$\eta^+(-x,y) = -\eta^+(x,y),\ \eta^-(-x,y) = \eta^-(x,y),$$
$$\eta^{\pm}(x,-y) = -\eta^{\pm}(x,y).$$

There is a discontinuity at the x axis in $\eta^{\pm}$:

$$\eta^+(x,0+) - \eta^+(x,0-) = 2\pi \text{ sign } x \text{ for } |x| > x_0,$$
$$\eta^-(x,0+) - \eta^-(x,0-) = 2\pi \text{ for } |x| < x_0.$$

Regarding the coordinate $\eta^{\pm}$ as a cyclic variable, this discontinuity is removed. However, $\eta^{\pm}$ remains discontinuous at the current sheets. The coordinate $\mu^{\pm}$ is continuous everywhere.

Figure 1b and d show the coordinates $\mu^{\pm}$ (thick red lines) and $\eta^{\pm}$ (thin blue lines). These figures are very similar to corresponding figures of the uniform-current case (Romashets and Vandas, 2012), so labeling is nearly the same. Both coordinates are displayed with step of 0.25. The coordinate μ^+ (Fig. 1b) is labeled vertically in the belt between $\eta^+ = -0.5$ and -0.25 from 2 to 4; an additional value of 2 is in the belt between $\eta^+ = 0.25$ and 0.5. The coordinate η^+ is labeled clockwise in the belt between $\mu^+ = 3.25$ and 4 from -3 to 3. The y axis has $\eta^+ = 0$, and the x axis has $\eta^+ = \pm\pi$ for $|x| > x_0$ (the places of discontinuity are plotted by the thin blue dashed lines) and value 0 between $-x_0$ and x_0 (see additional digit 0 there). The μ^- (Fig. 1d) is labeled clockwise in the belt between $\eta^- = 0.5$ and 0.75 from -1 to 1. The y axis has $\mu^- = 0$. The η^- is labeled vertically in the belt between $\mu^- = -0.5$ and -0.25 (with exception of the value 0 at the x axis). The x axis has $\eta^- = 0$ for $|x| > x_0$ and $\pm\pi$ between $-x_0$ and x_0 (again, the place of discontinuity is plotted by the thin blue dashed line). One can see that there are only minor differences between Fig. 1 and its limiting case $y_1 = y_0$ (Fig. 1 of Romashets and Vandas, 2012).

To construct the pair $\alpha^{\pm}$, $\beta^{\pm}$ we set

$$\alpha^{\pm} = B_i x_0 z + B_0 x_0^2 f^{\pm}(\mu^{\pm}, \eta^{\pm}), \quad (17)$$
$$\beta^{\pm} = \mu^{\pm}, \quad (18)$$

where

$$f^{\pm} = \frac{1}{x_0^2} \int_0^{\eta^{\pm}} \left[\left(\frac{\partial \mu^{\pm}}{\partial x} \right)^2 + \left(\frac{\partial \mu^{\pm}}{\partial y} \right)^2 \right]^{-1} \mathrm{d}\eta'^{\pm}$$

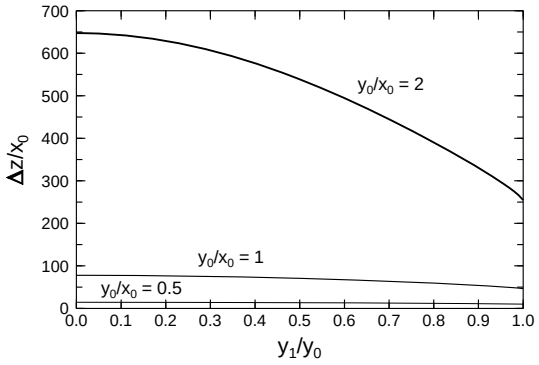

Figure 3. Lead Δz of magnetic field lines as a function of y_1 for three sheet widths in anti-parallel case.

$$= B_i^2 \int_0^{\eta^{\pm}} \frac{\mathrm{d}\eta'^{\pm}}{(B_x^{\pm})^2 + (B_y^{\pm})^2} \quad (19)$$

(cf. Romashets and Vandas, 2012). The integration is for a constant $\mu^{\pm}$, i.e., along a magnetic field line ($\eta'^{\pm}$ parameterizes the line). The thick red lines in Fig. 1b and d also are projections of magnetic field lines which are helical in the z direction and lie on magnetic surfaces defined by $\mu^{\pm} = \text{const}$. To check our derivation, we compared these lines with magnetic field lines following from the direct numerical integration using the field (Eq. 9). They were coincident.

3 Comparison to sheets with uniformly distributed currents

We shall consider anti-parallel case, which has relevance to Birkeland currents, and drop "$-$" from quantities for clarity. For calculations we took the same values of constants in the model as used in Romashets and Vandas (2012): $B_0 = 60\,000$ nT, $B_i = 6000$ nT, and $x_0 = 150$ km. The relatively high value of B_i represents a hypothetic geomagnetic superstorm.

Figure 3 shows lead Δz of helical magnetic field lines as a function of y_1 for three sheet widths y_0 (Δz is the length along the z axis over which the field line makes a full rotation). Solid lines are labeled by their y_0 values and their thickness increases with increasing y_0. All profiles are for one particular magnetic field line, that is, the line which crosses the edge of the sheet. One can see that when y_0 increases, the field lines become less helical. For a given y_0 the lead Δz decreases with y_1, but for lower y_0 it is nearly constant. The values of Δz at the limit $y_1 = y_0$ coincide with places of bullets which can be found in Fig. 2 of Romashets and Vandas (2012); μ slightly changes along each profile, increases with rising y_1, approximately from 1.53 to 1.73 for $y_0 = x_0/2$, from 0.93 to 1.13 for $y_0 = x_0$, and from 0.46 to 0.66 for $y_0 = 2x_0$.

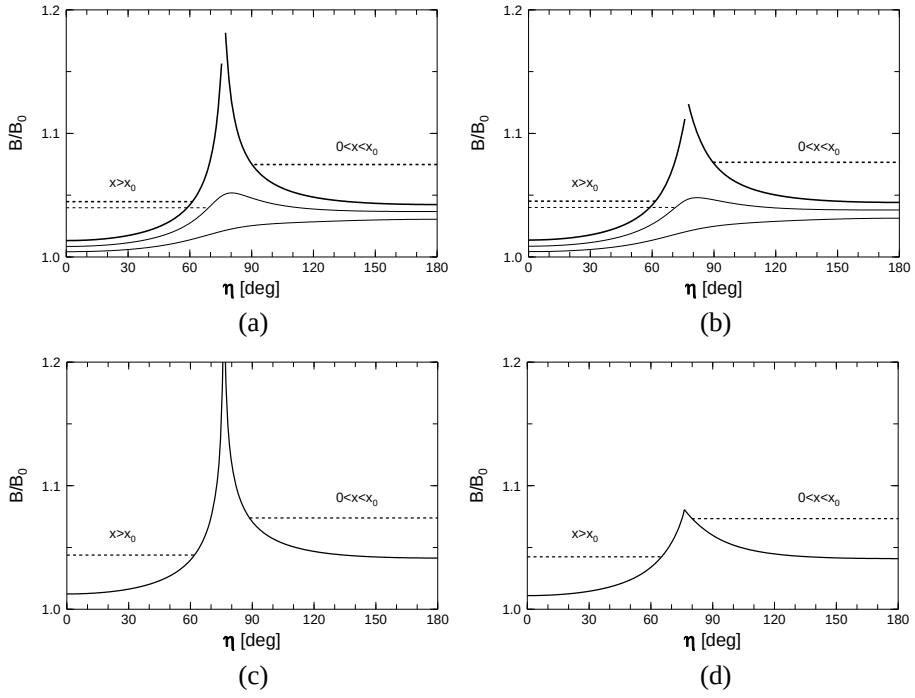

Figure 4. B profiles along magnetic field lines for $y_0 = x_0/2$ (anti-parallel case). Top: three field lines when **(a)** $y_1 = y_0$ (taken from Romashets and Vandas, 2012) or **(b)** $y_1 = 0.9y_0$. Bottom panels: **(c, d)** supplements **(a, b)**, respectively, with magnetic field lines crossing an edge of a sheet. The dashed lines show mirroring condition for particles with initial pitch angle 80°; their thickness corresponds to associated magnetic field lines.

Examples of particle mirroring at magnetic field lines for $y_0 = x_0/2$ are shown in Fig. 4. Figure 4a is taken from Romashets and Vandas (2012) (Fig. 3b there) and represents the limiting case $y_1 = y_0$. Figure 4b is made in the same format, but for $y_1 = 0.9y_0$. Magnetic field magnitude profiles along three magnetic field lines are plotted by lines with different thicknesses. The dashed lines show mirroring condition (level of magnetic field magnitude at which particles mirror) for particles with initial pitch angle 80° (the angle between the particle velocity and the magnetic field vector), the particles start from the x axis. The line thickness corresponds to associated magnetic field lines. The thick line is for a magnetic field line with $\cosh\mu = 3$ ($\mu \doteq 1.763$). It crosses the sheet, which is manifested as a jump in B and η. Particles mirror in both regions, $x > x_0$ and $x < x_0$, and there are two associated dashed lines (with different levels of mirror B). A magnetic field line with $\cosh\mu = 2.5$ ($\mu \doteq 1.567$) is plotted by the line with normal thickness. It does not cross the sheet but has a local B maximum near $x = x_0$. Our particles mirror only in the region $x > x_0$. The thin line represents a more distant magnetic field line with $\cosh\mu = 2$ ($\mu \doteq 1.317$). It has only one B maximum (at the x axis). Here our particles do not mirror. Comparison of Fig. 4a and b indicates that they are quite similar. These figures are supplemented by Fig. 4c and d, showing magnetic-field-line profiles for lines crossing an edge of a sheet. Figure 4c displays the limiting case $y_1 = y_0$ as Fig. 4a above it ($\mu \doteq 1.730$, cf. description of Fig. 3), while Fig. 4d is for $y_1 = 0.9y_0$ like Fig. 4b ($\mu \doteq 1.665$). The magnetic field profiles are very different. The magnitude in Fig. 4c rises to infinity, contrary to Fig. 4d, where its maximum is even lower than in Fig. 4b. Nevertheless conditions for mirroring are quite similar. For slightly higher pitch angles the particles would not mirror in the present case (Fig. 4d) while in the former they do (Fig. 4c). So only a tiny fraction of particles which reach a very vicinity of the edges will mirror differently. Therefore results and conclusions of Romashets and Vandas (2012) remain valid.

Figure 5 displays magnetic field magnitude at the sheet edges as a function of y_1 for three sheet widths y_0. As in Fig. 3, the lines are labeled by their y_0 values and their width indicates the value of y_0. Magnetic field value remains nearly constant for a wide range of y_1 values. For y_0 comparable to x_0 and larger the field magnitude starts to rise to infinity when y_1 is very close to y_0.

Figure 1e shows the situation with magnetic field magnitude near a sheet edge in more detail. It is a magnified part of Fig. 1c around the sheet edge described by the point $[x_0, y_0]$. Magnetic field maximum is not situated at the edge but shifted towards the point where the current density begins to drop, that is, the place with coordinates $[x_0, y_1]$ and stressed by the bullet in the figure.

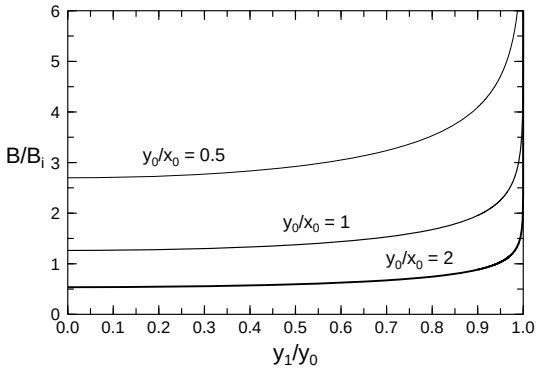

Figure 5. Magnetic field magnitude at the sheet edges as a function of y_1 for three values of the sheet widths y_0 (anti-parallel case).

The current density along the sheet (Fig. 2) is not smooth. Using a higher-order polynomial, we can make it smooth. For example,

$$j_z = \frac{j_0}{(y_0 - y_1)^3}\Big[2|y|^3 - 3(y_0 + y_1)y^2 + 6y_0 y_1 |y| + y_0^2(y_0 - 3y_1)\Big] \tag{20}$$

for $y_1 < |y| < y_0$, the profile of which is shown in Fig. 6 by the thick line. It is possible to go through the procedures described above and to derive Euler potentials for such a system, but the calculations would be more complex.

4 Hypothetic observations of magnetic field and particle flux variations

In order to compare effects on charged particles of the current systems with zero and non-zero sheet thicknesses, we investigate particle flux variations which would observe a hypothetic spacecraft moving perpendicularly through the sheets. Besides the comparison, the simulated observations may serve as examples of what a spacecraft could measure during a superstorm. At present, such observations are not available because no superstorm with a strength comparable to the 1859 Carrington event (Tsurutani et al., 2003; Siscoe et al., 2006) occurred during the cosmic era.

Consider charged particles moving adiabatically in a magnetic field system. The number density of the particles is given by

$$n = \int_0^\infty \int_0^\pi \int_0^{2\pi} f(v, \alpha, \varphi)\, v^2 \sin\alpha \, \mathrm{d}\varphi \, \mathrm{d}\alpha \, \mathrm{d}v, \tag{21}$$

where f is the particle distribution function, v is the velocity magnitude, α is the pitch angle, and φ is the phase. A hemispheric flux of these particles along the magnetic field vector

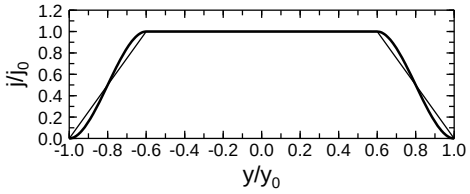

Figure 6. Profiles of the surface current density j along a sheet. The thick line is a profile which is smooth; that is, it has zero derivatives at $\pm y_1$ and $\pm y_0$ ($y_1 = 0.6y_0$ in the plot). The thinner line is the trapezoidal profile used in the current paper (cf. Fig. 2) and it is shown for a comparison.

reads

$$F = \int_0^\infty \int_0^{\frac{\pi}{2}} \int_0^{2\pi} f(v, \alpha, \varphi)\, v^3 \sin\alpha \cos\alpha \, \mathrm{d}\varphi \, \mathrm{d}\alpha \, \mathrm{d}v. \tag{22}$$

Let us assume that the initial distribution function is a monoenergetic gyrotropic distribution with a simple anisotropy

$$f_0(v, \alpha, \varphi) = \frac{n_0}{4\pi v_0^2}(1 + A_1 \cos\alpha)\delta(v - v_0), \tag{23}$$

where n_0 is the particle number density, v_0 is the particle velocity, A_1 is a coefficient determining anisotropy, and δ is the delta function. The hemispheric flux for this distribution function is given by

$$F_0 = \frac{3 + 2A_1}{12} n_0 v_0. \tag{24}$$

Figure 7 schematically shows a magnetic field line. It is drawn by a straight line only for simplicity, and it may be curved. The direction of the field vector $\boldsymbol{B}$ is indicated by the left arrow. The right bullet locates the global magnetic field maximum along the given field line with its value B_m and the particle flux F_m. A general point where a hypothetic spacecraft observes is drawn by the left bullet and labeled by B_1 and F_1. At this point, the meaning of the hemispheric flux is sketched by a semicircle. The background field is far right with its value B_0 and the corresponding initial flux F_0. In our system, magnetic field lines are oriented vertically, so the right arrow in Fig. 7 points to increasing height (z direction).

The hemispheric flux along the field line is calculated using the Liouville theorem. The flux F_m is

$$F_\mathrm{m} = \int_0^\infty \int_0^{\frac{\pi}{2}} \int_0^{2\pi} f_0[v, \arcsin(\sqrt{B_0/B_\mathrm{m}}\sin\alpha), \varphi]\, v^3 \times \sin\alpha \cos\alpha \, \mathrm{d}\varphi \, \mathrm{d}\alpha \, \mathrm{d}v \tag{25}$$

and the flux F_1 is

$$F_1 = \int_0^{\infty} \int_0^{\arcsin(\sqrt{B_1/B_\mathrm{m}})} \int_0^{2\pi} f_0[v, \arcsin(\sqrt{B_0/B_1}\sin\alpha), \varphi]\, v^3$$

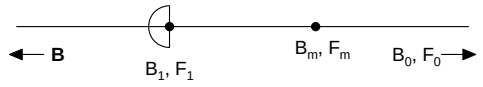

Figure 7. Sketch of a magnetic field line with values of magnetic field magnitudes B and hemispheric fluxes F at several locations. Further explanation is given in the text.

$$\times \sin\alpha \cos\alpha \, \mathrm{d}\varphi \, \mathrm{d}\alpha \, \mathrm{d}v, \tag{26}$$

so we get

$$\frac{F_1}{F_0} = \frac{3b_{0\mathrm{m}} + 2A_1[1-(1-b_{0\mathrm{m}})^{\frac{3}{2}}]}{b_{01}(3+2A_1)}, \tag{27}$$

where $b_{0\mathrm{m}} = B_0/B_\mathrm{m}$ and $b_{01} = B_0/B_1$. Equations (26)–(27) were derived under the assumption that the observation point is behind the field maximum (as it is drawn in Fig. 7). Because our system is periodic, this condition is always fulfilled. However, strictly speaking, due to this periodicity, the asymptotic value B_0 is not reached like it is indicated by the right arrow. But in a real situation, the sheets are limited in z, and far from them (in the direction of the right arrow) there is the asymptotic value B_0.

For the initially isotropic distribution ($A_1 = 0$) we have

$$\frac{F_1}{F_0} = \frac{B_1}{B_\mathrm{m}}. \tag{28}$$

So, in this case, the flux at the field maximum is the same as the initial one.

Figure 8 shows magnetic field and particle flux variations when a spacecraft moves along the x axis: it crosses the sheets perpendicularly and in the middle. There are six panels in the figure, and each panel consists of three graphs, showing the relative values of (top) magnetic field magnitude B, (middle) field component generated by the sheets, B_y, and (bottom) hemispheric particle flux F_1 with respect to the background values (with subscripts 0). There are two lines in the bottom graphs: the thicker line is for an initially isotropic distribution, the thinner one for an anisotropic distribution. The vertical dashed lines are positions of the sheets or their edges (for non-zero thickness). Figure 8a is for the system of sheets with a non-uniform current density and zero thickness (model described in this paper). The sheets have parameters $y_0/x_0 = 1/2$ and $y_1/y_0 = 0.9$. The presence of the sheets is pronounced in all shown profiles, the magnetic field magnitude, the component generated by the sheets (it is B_y, the other components are $B_x = 0$ and $B_z = B_0$), and the hemispheric particle flux. The latter quantity is plotted for two cases: for the initially isotropic distribution and for the anisotropic distribution with $A_1 = 1/3$. These two profiles are quite similar; they have flux depressions on both sides of the sheets. This is due to the fact that the spacecraft meets the same field lines in front of and behind the sheet, so B_m is the same but B_1 differs for a particular line (cf. Eq. 28). Therefore the depression repeats, but not exactly with the same profile.

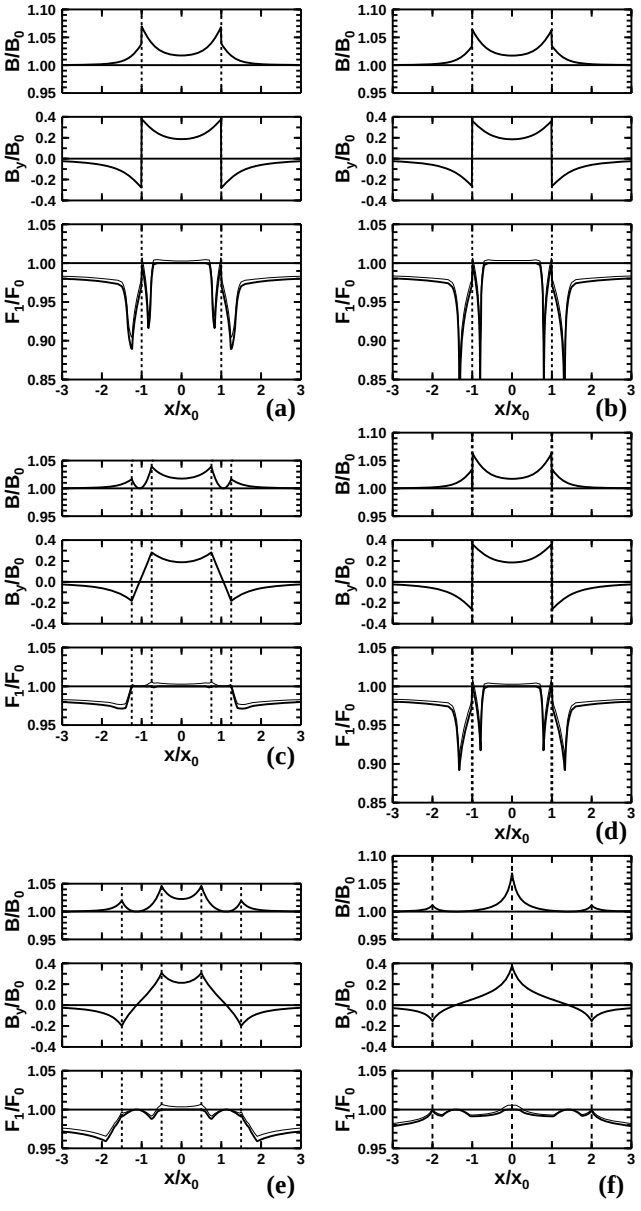

Figure 8. Magnetic field and particle flux variations near the sheets. B is the magnetic field magnitude, B_y is the field component generated by the sheets, and F_1 is the hemispheric particle flux. Details are given in the text.

Changing y_1 to a limiting case $y_1 = 0.999y_0$ (approaching case with a uniform current distribution, covered in Romashets and Vandas, 2012), we get what is shown in Fig. 8b. Depressions are deeper because the field magnitude is higher near the edges. The flux variations are very similar in Fig. 8a and b elsewhere.

Figure 8c complements Fig. 8a. The sheets have the same $y_0/x_0 = 1/2$ but the non-zero thickness $d_0/x_0 = 1/4$ and a

uniform current density, so the solution by Vandas and Romashets (2014) is used. Magnetic field variations are smaller than in Fig. 8a because the current is more diluted. Also the flux variations are smaller and qualitatively different. But if the thickness becomes small, $d_0/x_0 = 1/100$, this case, shown in Fig. 8d, approaches the one displayed in Fig. 8b. Only the flux depressions are not so deep, but they resemble that in Fig. 8a because of the non-zero sheet thickness.

Figure 8e shows the case with the sheets of non-zero thickness and a uniform current, when the sheets are prolate (resemble filaments): $y_0/x_0 = 1/4$ and $d_0/x_0 = 1/2$, i.e., $d_0 > y_0$. In fact, the values of y_0 and d_0 are swapped from the case of Fig. 8c. The variations become larger in comparison with this figure.

The B_y profiles have a general behavior during the passage of the sheets (Fig. 8a–e): the component has one polarity, it reverses and becomes comparable or larger (in the absolute value) between the sheets, and finally it reverses again. There is a dip between the sheets, which depends (among others) on the sheet separation distance; if it is smaller, the dip is smaller. This behavior is qualitatively in agreement with observations of a disturbed magnetic field component. See for instance Figs. 3 and 4 by Armstrong and Zmuda (1973) or Fig. 2b by Waters et al. (2001). In the last figure, there is no dip in the field. In our model, it occurs when the sheets are in contact, as shown in Fig. 8f (model by Vandas and Romashets, 2014, with $d_0 = x_0$). However, quantitatively this figure is different from Fig. 2b in Waters et al. (2001), for our values of the disturbed component are 1 order of magnitude larger. These high values are necessary for non-negligible variations of particle fluxes along magnetic field lines. They were achieved by a relatively high value of B_i (10 % of the background value). That is why we speak of a superstorm (of the Carrington event caliber) when there could be measurable effects on energetic-particle fluxes. In common storm conditions, flux variations would be below 1 % and probably masked by other effects.

5 Conclusions

In a previous work (Romashets and Vandas, 2012), Euler potentials of two current sheets of finite width and zero thickness, aligned to a uniform ambient magnetic field, were presented. Electric surface currents were uniformly distributed on the sheets. However, for this system, the magnetic field reaches infinite values at the sheet edges, and it raises the question of its applicability to real systems.

In the present paper, we consider a current distribution in which the current falls to zero at the edges (in a trapezoidal profile). This removes the field divergence while retaining the field configuration very close to the former one. Therefore former results and conclusions of Romashets and Vandas (2012) are valid and applicable to the more realistic model presented in this work. In addition, this is also emphasized by an important conclusion from the new model – that for the current sheet widths larger than their separation ($y_0 > x_0$), magnetic field configuration becomes insensitive to the position where the current starts to drop (value y_1 of the model). The model described in this work can serve as a simple model for Birkeland currents, namely as a local model when they have a filamentary structure. We emphasize a local model, because in such an environment simple assumptions as a planar geometry of the sheets and a background homogeneous magnetic field might be justifiable. These simple assumptions are necessary for our analytical approach. And analytical results are much more flexible for calculations when initial parameters change. In principle, the method used here can be applied to a system of local sheets (filaments), but the treatment would be much more complex.

Using Euler potentials we investigated the influence of current sheets of zero and non-zero thicknesses on energetic-particle fluxes and analyzed their characteristic variations near the sheets. The variations might serve as a tool to reveal geometric parameters of the sheets. Figure 8 shows characteristic field and particle-flux profiles for selected geometries. The particle-flux variations in the vicinity of the sheets are pronounced only for very disturbed periods, like in a geomagnetic superstorm.

Acknowledgements. This work is supported by project 14-19376S from GA ČR. We also acknowledge support from the AV ČR grant RVO:67985815.

The topical editor, E. Roussos, thanks two anonymous referees for their help in evaluating this paper.

References

Anderson, B. J., Korth, H., Waters, C. L., Green, D. L., Merkin, V. G., Barnes, R. J., and Dyrud, L. P.: Development of large-scale Birkeland currents determined from the active magnetosphere and planetary electrodynamics response experiment, Geophys. Res. Lett., 41, 3017–3025, doi:10.1002/2014GL059941, 2014.

Armstrong, J. C. and Zmuda, A. J.: Triaxial magnetic measurements of field-aligned currents at 800 kilometers in the auroral region: Initial results, J. Geophys. Res., 78, 6802–6807, 1973.

Euler, L.: Principiis Motus Fluidorum, Novi Comentarii Acad. Sci. Petropolitanae, 14, 270–284 (reprinted in Physica D: Nonlinear Phenomena, 237, 1840–1854, 2008), 1769.

Friis-Christensen, E. and Lassen, K.: Large-scale distribution of discrete auroras and field aligned currents, in: Auroral Physics, edited by: Meng, C.-I., Rycroft, M. J., and Frank, L. A., 369–381, Cambridge University Press, New York, 1991.

Gardner, C. S.: Adiabatic invariants of periodic classical systems, Phys. Rev., 115, 791–794, 1959.

Gkioulidou, M., Wang, C.-P., Wing, S., Lyons, L. R., Wolf, R. A., and Hsu, T.-S.: Effect of an MLT dependent electron loss rate on the magnetosphere-ionosphere coupling, J. Geophys. Res., 117, A11218, doi:10.1029/2012JA018032, 2012.

Iijima, T. and Potemra, T. A.: The amplitude distribution of field-aligned currents at northern high latitudes observed by Triad, J. Geophys. Res., 81, 2165–2174, 1976a.

Iijima, T. and Potemra, T. A.: Field-aligned currents in the dayside cusp observed by Triad, J. Geophys. Res., 81, 5971–5979, 1976b.

Korth, H., Anderson, B. J., and Waters, C. L.: Statistical analysis of the dependence of large-scale Birkeland currents on solar wind parameters, Ann. Geophys., 28, 515–530, doi:10.5194/angeo-28-515-2010, 2010.

Northrop, T. and Teller, E.: Stability of the adiabatic motion of charged particles in the Earth's field, Phys. Rev., 117, 215–225, 1960.

Ray, E.: On the motion of charged particles in the geomagnetic field, Ann. Phys., 24, 1–18, 1963.

Romashets, E. and Vandas, M.: Euler potentials for two current sheets along ambient uniform magnetic field, J. Geophys. Res., 117, A07221, doi:10.1029/2012JA017587, 2012.

Russell, C. T. and Fleishman, M.: Joint control of region-2 field-aligned currents by the east-west component of the interplanetary electric field and polar cap illumination, J. Atmos. Sol.-Terr. Phy., 64, 1803–1808, 2002.

Russell, C. T., Zhou, X.-W., Le, G., Reiff, P. H., Luhmann, J. G., Cattell, C. A., and Kawano, H.: Field aligned currents in the high latitude, high altitude magnetosphere: POLAR initial results, Geophys. Res. Lett., 24, 1455–1458, 1997.

Schield, M. A., Freeman, J. W., and Dessler, J.: A source for field-aligned currents at auroral latitudes, J. Geophys. Res., 74, 247–256, 1969.

Schulz, M. and Chen, M.: Field-line (Euler-potential) model of the ring current, J. Atm. Sol.-Terr. Phy., 70, 482–489, 2008.

Siscoe, G., Crooker, N. U., and Clauer, C. R.: Dst of the Carrington storm of 1859, Adv. Space Res., 38, 173–179, 2006.

Stern, D. P.: The motion of magnetic field lines, Space Sci. Rev., 6, 147–173, 1966.

Sweet, P. A.: The effect of turbulence on magnetic field, Mon. Not. R. Astron. Soc., 110, 69–83, 1950.

Tsurutani, B. T., Gonzalez, W. D., Lakhina, G. S., and Alex, S.: The extreme magnetic storm of 1–2 September 1859, J. Geophys. Res., 108, 1268, doi:10.1029/2002JA009504, 2003.

Vandas, M. and Romashets, E. P.: Euler potentials for two current sheets of nonzero thickness along ambient uniform magnetic field, J. Geophys. Res., 119, 2579–2592, doi:10.1002/2013JA019604, 2014.

Vasyliunas, V. M.: Mathematical models of magnetospheric convection and its coupling to the ionosphere, in: Particles and Fluids in the Magnetosphere, edited by: McCormac, B. M., 60–71, D. Reidel, Hingham, Mass., 1970.

Wang, C.-P., Gkioulidou, M., Lyons, L. R., Xing, X., and Wolf, R. A.: Interchange motion as a transport mechanism for formation of cold-dense plasma sheet, J. Geophys. Res., 119, A11218, doi:10.1002/2014JA020251, 2014.

Waters, C. L., Anderson, B. J., and Liou, K.: Estimation of global field aligned currents using the Iridium system magnetometer data, Geophys. Res. Lett., 28, 2165–2168, 2001.

Webb, G. M., Hu, Q., Dasgupta, B., and Zank, G. P.: Homotopy formulas for the magnetic vector potential and magnetic helicity: The Parker spiral interplanetary magnetic field and magnetic flux ropes, J. Geophys. Res., 115, A10112, doi:10.1029/2010JA015513, 2010.

Zaharia, S.: Improved Euler potential method for three-dimensional magnetospheric equilibrium, J. Geophys. Res., 113, A08221, doi:10.1029/2008JA013325, 2008.

Zmuda, A. J. and Armstrong, J. C.: The diurnal flow pattern of field-aligned currents, J. Geophys. Res., 79, 4611–4619, 1974.